Electronic Supplementary Material (ESI) for Journal of Materials Chemistry A.
This journal is © The Royal Society of Chemistry 2016

Electronic Supplementary Information

Decoration of the inert basal plane of defect-rich MoS_2 with Pd atoms for achieving Pt-similar HER activity

Kun Qi, Shansheng Yu, Qiyu Wang, Wei Zhang, Jinchang Fan, Weitao Zheng, and Xiaoqiang Cui**

Department of Materials Science, Key Laboratory of Automobile Materials of MOE and State Key Laboratory of Superhard Materials, Jilin University, Changchun 130012, Jilin, People's Republic of China.

E-mail: xqcui@jlu.edu.cn (X. Q. Cui); wtzheng@jlu.edu.cn (W. T. Zheng)

Contents

DFT Calculation details:

1. ***Construction of the infinite stripe model of MoS_2 unit cell:***

Figure. S1 Unit cell of the MoS_2 slab

2. ***Hydrogen binding free energy on Pd-MoS_2 system:***

Figure. S2 Geometric fragments of Pd-MoS_2 with hydrogen atoms adsorbed on the edge

Table. S1 Calculated Gibbs free energy of hydrogen adsorption in the palladium-adsorbed MoS_2 slab

3. ***Hydrogen binding free energy on pristine MoS_2 system:***

Figure. S3 Geometric fragments of pristine MoS_2 with hydrogen atoms adsorbed on the edge

Table. S2 Calculated Gibbs free energy of hydrogen adsorption in the pristine MoS_2 slab

4. ***Comparasion of the hydrogen binding free energy on Pd-MoS_2 and pristine MoS_2 systems:***

Figure. S4 Calculated Gibbs free energy graph of hydrogen adsorption

Experimental Section:

1. ***Materials and reagents:***
2. ***Characterization:***
3. ***Epitaxial growth and assembly of Pd-NPs for the preparation of Pd-MoS_2 heterostructures:***
4. ***Synthesis and characterization of defect-rich MoS_2 nanosheets:***

Figure. S5 Characterization of defect-rich MoS_2 nanosheets (DR-MoS_2)

5. ***Synthesis, characterization and the exploration of the formation mechanism for Pd nanodisks:***

Figure. S6 TEM images Pd nanodisks (Pd NDs) with different rotation angles
Figure. S7 Characterization of Pd hexagon nanosheets
Figure. S8 Characterization of Pd polyhedral
Figure. S9 Routes for the synthesizing of Pd nanostructures by controlling CO / Air ratio

6. ***Assembly of Pd nanodisks on MoS_2 nanosheets:***

Figure. S10 Zeta-potential of Pd NDs and DR-MoS_2 nanosheets
Figure. S11 Strategies for the combination of Pd NDs and DR-MoS_2 nanosheets
Figure. S12 XPS spectra of DR-MoS_2 nanosheets sonicated in the absence of Pd NDs

7. ***Electrochemical measurements and further characterizations after stability tests:***

Figure. S13 Optical photographs of the hydrogen bubbles generating during HER process
Figure. S14 TEM images of Pd NDs/DR-MoS_2 heterostructure after stability test
Figure. S15 XPS spectra of Pd NDs/DR-MoS_2 heterostructure after stability test
Table. S3 HER parameters of various samples in this work
Table. S4 Calculations of the exchange current densities of various samples in this work

DFT Calculation details

1. Construction of the infinite stripe model of MoS_2 unit cell:

All theoretical calculations were conducted using density functional theory (DFT) by DMOL3 code.[1, 2] In the DFT calculations, the all-electron Kohn–Sham wave functions were expanded in the double numerical polarized atomic orbital basis, and the generalized gradient approximation with the Perdew–Burke–Ernzerh of describing the exchange and correlation energy was employed.[3] Self-consistent field procedure was done until the change of energy was less than 10^{-6} Hartree, and the geometrical optimization of the structure was done with an energy convergence criterion of 10^{-5} Hartree. Long range nonlocal effects were taken into account by applying van der Waals dispersion corrections through the DFT-D scheme with Grimme parameters, whose S6=0.75.[4] In atomic parameters, C_6 for H, S, Mo and Pd is chosen to be 1.451, 57.729, 255.687 and 255.687 eVÅ, and the vdW radious R0 is set as 1.001, 1.683, 1.639 and 1.639 Å, respectively. In order to make a comparison with previous literatures,[5, 6] the systems have been constructed with the infinite stripe model in Figure S1, which are four Mo atoms wide in x-direction and six Mo atoms wide in y-direction. The experimental in-plane lattice constant of 3.16Å for the in-plane unit cell of MoS_2 monolayers has been used. Using periodic boundary conditions, the unit cell dimension in x-direction is 12.64 Å, in y-direction 30 Å and in z-direction 30 Å. A vacuum region is enough to ensure negligible interaction between the infinite slab and its periodic images. In the infinite slab, both the S-edge and the Mo-edge are exposed, and the Mo-edge is the edge present in the catalytic particles. Under the employed reaction conditions, the nanoparticles are terminated by the Mo-edge with sulfur monomers.[5, 7] Since the S-edge is not present in the catalytic particles, the exact configuration of the S-edge is kept constant which is irrelevant in the calculations. The

spin-unrestricted calculations were carried out. The Brillouin zone was sampled by Monkhorst-Pack 3×1×1 and 12×1×1 k-point grid for geometrical optimization and total energy.[8]

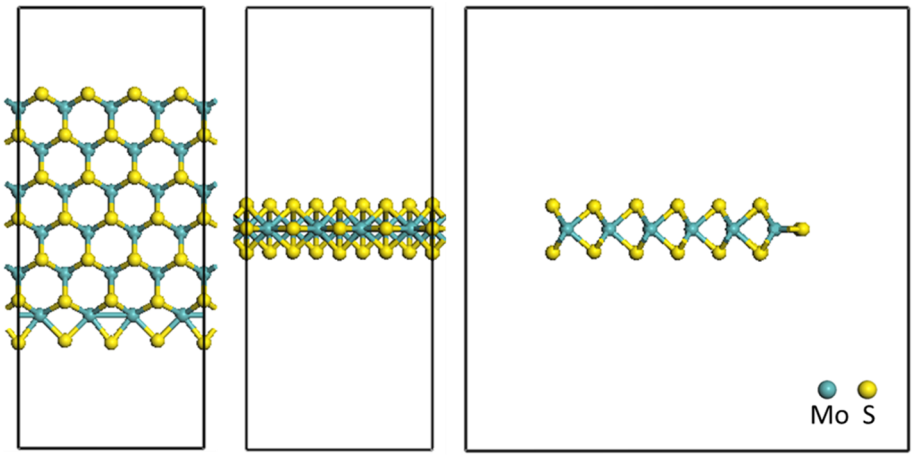

Figure S1. The top, front and side views of the unit cell for the MoS_2 slab are exhibited, in which the Mo-edge is terminated by sulfur monomers.

2. Hydrogen binding free energy on Pd-MoS_2 system:

The stability of hydrogen can be defined by the differential hydrogen adsorption energy as described by previous studies,[5, 6, 9] which is calculated as follows:

$$\Delta E_{\mathrm{H}} = E(\mathrm{slab} + n\mathrm{H}) - E(\mathrm{slab}+(n-1)\mathrm{H}) - \frac{1}{2}E(\mathrm{H}_2) \qquad (1)$$

where $E(\mathrm{slab} + n\mathrm{H})$ is the total energy for the pristine or metal-adsorbed MoS_2 slab with n hydrogen atoms adsorbed on the edge. $E(\mathrm{slab} + (n-1)\mathrm{H})$ is the total energy for (n-1) hydrogen atoms adsorbed on the edge, and $E(H_2)$ is the energy for a hydrogen molecule in the gas phase. The ΔE_{H} obtained from the ground state calculations does not include the contributions from the vibrational motion and the entropy. The calculation methodology for the Gibbs free energies of hydrogen adsorption is specified in Ref. 5. Therefore, according to Ref. 5, the differential hydrogen binding free energies can be determined as $\Delta G_{\mathrm{H}} = \Delta E_{\mathrm{H}} + 0.29\mathrm{eV}$ for our models. The differential hydrogen binding free energy describes the energy needed to increase the coverage by one hydrogen atom, which is a good descriptor for hydrogen evolution reaction (HER). Our model slab is four rows of Mo wide and therefore we have four hydrogen binding sites and can describe the coverage 25%, 50%, 75% and 100% which have two, three, two and one types of hydrogen arrangements on the edge for the pristine MoS_2 slab in Figure S4 while three, four, three and one types of hydrogen arrangement on the edge for the palladium-adsorbed MoS_2 slab in Figure S2, respectively. ΔG_{H} is defined such that the value for 1/4 indicates, how much energy is required for increasing the coverage from 0 to 25%, the value for 2/4 indicates, how much energy is required to increase the coverage from 25% to 50%, and similar for the other coverage. Consequently, there exist two, four, four and two configurations from (n-1) hydrogen adsorption system to n hydrogen adsorption system for 1/4, 2/4, 3/4 and 4/4 in the pristine MoS_2 slab in Table S2 while three, seven, seven and three configurations for 1/4, 2/4, 3/4 and 4/4 in the palladium-adsorbed MoS_2 slab in Table S1. The

values of calculated ΔG_{H} are exhibited in Table S1, Table S2 and Figure S4. It is clear that the hydrogen generally prefers to bind on the edge at low coverage.

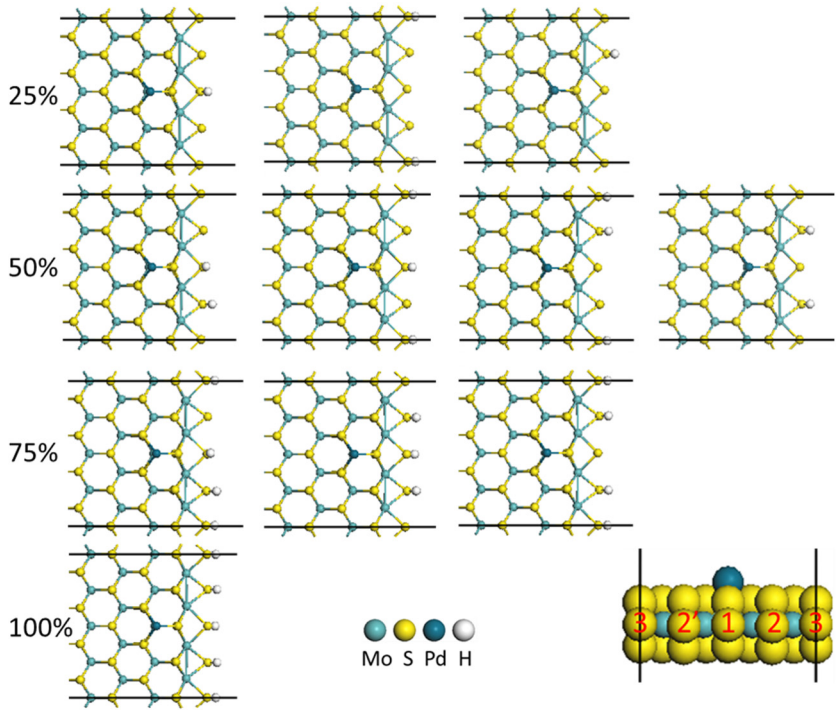

Figure S2. For the palladium-adsorbed MoS_2 slab, the geometric fragments on the edge adsorbed with one, two, three and four hydrogen atoms from up to down are shown, respectively. Inset: the numbers on the S edge indicate the sites of hydrogen binding, in which there are three nonequivalent sites 1, 2(2') and 3 in the slab owing to palladium adsorption.

Table S1. Calculated Gibbs free energy of hydrogen adsorption for 1/4, 2/4, 3/4 and 4/4 in the palladium-adsorbed MoS_2 slab. The numbers in the brackets indicate the sites which hydrogen atoms have bound, and the number out the brackets is the site which one hydrogen atom intends to bind.

1/4	1	2	3				
ΔG_{H}(eV)	-0.28	0.03	-0.29				
2/4	[1],2	[1],3	[2],1	[2],2'	[2],3	[3],2	[3],1
ΔG_{H}(eV)	0.32	-0.11	0.01	0.1	-0.14	0.18	-0.10
3/4	[1,2],3	[1,2],2'	[1,3],2	[2,2'],1	[2,2'],3	[2,3],1	[2,3],2'
ΔG_{H}(eV)	-0.07	0.10	0.37	0.01	-0.02	0.08	0.22
4/4	[1,2,3],2'	[1,2,2'],3	[2,2',3],1				
ΔG_{H}(eV)	0.17	0.01	0.03				

3. Hydrogen binding free energy on pristine MoS_2 system:

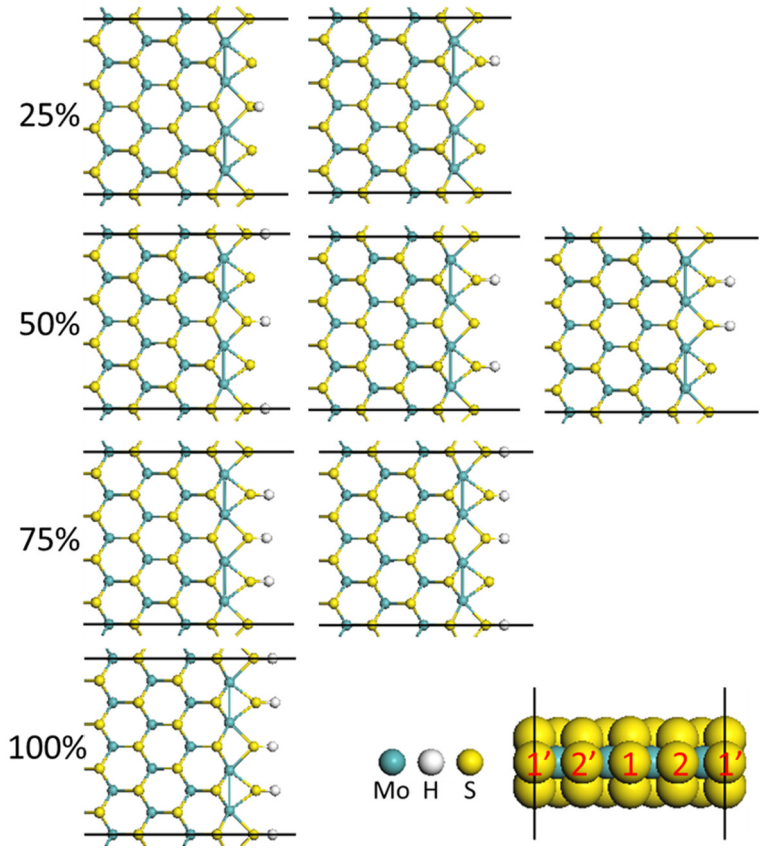

Figure S3. For the pristine MoS_2 slab, the geometric fragments on the edge adsorbed with one, two, three and four hydrogen atoms from up to down are shown, respectively. Inset: the numbers on the S edge indicate the sites of hydrogen binding, in which there are two nonequivalent sites 1(1') and 2(2') in the slab.

Table S2. Calculated Gibbs free energy of hydrogen adsorption for 1/4, 2/4, 3/4 and 4/4 in the pristine MoS_2 slab. The numbers in the brackets indicate the sites which hydrogen atoms have bound, and the number out the brackets is the site which one hydrogen atom intends to bind.

1/4	1	2		
ΔG_H(eV)	-0.32	-0.01		
2/4	[1],2	[1],1'	[2],1	[2],2'
ΔG_H(eV)	1.45	0.87	0.54	0.76
3/4	[1,2],1'	[1,2],2'	[1,1'],2	[2,2'],1
ΔG_H(eV)	0.77	1.17	1.36	0.95
4/4	[1,2,1'],2'	[1,2,2'],1'		
ΔG_H(eV)	1.38	1.08		

4. Comparasion of the hydrogen binding free energy on Pd-MoS_2 and pristine MoS_2 systems:

It was reported that the pristine MoS_2 slab possessed a small value of ΔG_H only for 2/4, viz., only for H coverage from 25% to 50%.[5, 6] In contrast, owing to considering long range nonlocal dispersion corrections, our calculations in Table S1 show the low energy barrier only for 1/4 in the pristine MoS_2 slab, which indicates that the HER process can only be driven at a very low H coverage. This result is agreement with our and other experimental studies providing that the HER performance of MoS_2 is not very well. In the palladium-adsorbed MoS_2 slab, it is noted that there exist small ΔG_H (-1~1 eV) for all coverage, as listed in Table S2 and Figure S4. Therefore, the HER process can be driven by hydrogen adsorption at all coverage. In addition, the mean value of $|\Delta G_H|$ for high H coverage is smaller than that for low H coverage, which indicates that the high H coverage can more effectively evolve hydrogen. More importantly, the palladium-adsorbed MoS_2 slab possesses much smaller ΔG_H at higher H coverage than that of the pristine MoS_2 counterpart in Figurer S4. It is predicated that the palladium-adsorbed MoS_2 catalyst can provide more effective sites and higher activity for HER process compared with the pristine MoS_2 catalyst. Consequently, the comparison of ΔG_H for H adsorption suggests that excellent HER performance could be possibly reached for the palladium-adsorbed MoS_2 catalyst.

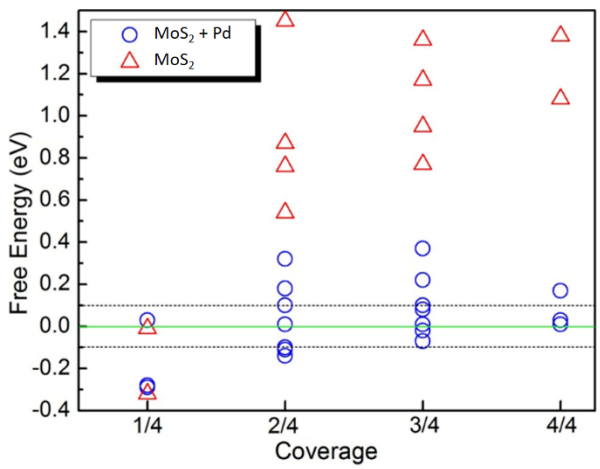

Figure S4. Calculated Gibbs free energy of hydrogen adsorption for 1/4, 2/4, 3/4 and 4/4.

Experimental Section

1. Materials and reagents:

Palladium acetylacetonate ($Pd(acac)_2$, 99%), Molybdenum sulphide (MoS_2, power), commercial Pt/C (10 wt. %) and Pd/C catalyst (10 wt. %) were obtained from Sigma-Aldrich. Sulphuric acid (H_2SO_4, AR) were obtained from Beijing chemical works, China. Cetyltrimethyl ammonium bromide (CTAB, AR), N,N-dimethylformamide (DMF, AR), Thiourea (AR), Hexaammonium heptamolybdate tetrahydrate ($(NH_4)_6Mo_7O_{24}\cdot 4H_2O$, AR) acetone (AR) and ethanol (AR) were all purchased from Sinopharm chemical reagent, China. Polyvinylpyrrolidone (PVP MW=50000, AR) were purchased from Aladdin reagent, China. Nitrogen, carbon oxide (ultra-purity) and air (high-purity) were purchased from Xin'guang gas Co., China. Nafion-ethanol solution was obtained from Adamas-beta Chemical Co., Switzerland. The water (18 MΩ cm^{-1}) used in all experiments was prepared by passing through an ultrapure purification system. All reagents were used as received without further purification.

2. Characterization:

Transmission electron microscope (TEM), high resolution transmission electron microscope (HRTEM) and selected area electron diffraction (SAED) were obtained using a JEM-2100F transmission electron microscope (JEOL Co., Japan). SEM images were taken with a Hitachi SU8000 scanning microscope at an accelerating voltage of 30 kV. X-Ray diffraction (XRD) patterns were acquired by using a Bragg-Brentano diffractometer (D8-tools, Germany), and the source was a Cu-Kα line at 0.15418 nm. X-ray photoelectron spectroscopy (XPS) data was acquired with an ESCALAB-250 instrument (Thermo Fisher Scientific, USA), performed with a monochromatic Al-Kα (1486.6 eV) radiation source and a hemisphere detector with an energy resolution of 0.1 eV. Zeta potentials of the as-prepared samples were determined by using a Zetasizer Nano ZS (Malvern Instruments Ltd., UK). Atomic force microscope (AFM) images were obtained by deposition of sample on freshly cleaved mica and investigated by using ScanAsyst in air with tapping mode (Dimension Icon, Veeco Instruments/Bruker, Germany). Fast Fourier transform (FFT) masked contrast refined HRTEM images were obtained by Gatan digital micrograph software. Sonication was performed in an ultrasonic cleaner with a frequency of 40 KHz and a nominal power of 800 W (KQ-800KDE, Kunshan ultrasonic instrument Co. Ltd.). The contact angle was measured on Kruss DSA30 contact angle system in ambient air at room temperature. Optical photographs were all acquired using an iPhone 6.

3. Epitaxial growth and assembly of Pd-NPs for the preparation of Pd-MoS_2 heterostructures:

3.1 Synthesis of Pd nanoparticles on MoS_2 by epitaxial growth:

In a typical synthesis, 300 μL MoS_2 (31.25 mM in ethanol) and 300 μL Na_2PdCl_4 (5.56 mM in ethanol) were dissolved by 10 mL ethanol in a glass vial with vigorously shocking. Then the vial was transferred to a constant temperature ultrasonic system with sonication for 36.0 h.

3.2 Synthesis of Pd nanoparticles on MoS_2 by sonification:

In a typical synthesis, Pd nanoparticles on MoS_2 by sonification were carried out by a two steps method. Pd nanoparticles were first obtained by a method reported in the literature before.[10] Then, 300 μL MoS_2 (31.25 mM in ethanol) and 300 μL Pd nanoparticles (5.56 mM in ethanol) were dissolved by 10 mL ethanol in a glass vial with vigorously shocking. Then the vial was transferred to a constant temperature ultrasonic system with sonication for 36.0 h.

4. Synthesis and characterization of defect-rich MoS_2 nanosheets:

Defect MoS_2 nanosheets were synthesized according to a published procedure. In a typical synthesis, 24.7 mg $(NH_4)_6Mo_7O_{24}\cdot 4H_2O$ and 53.2 mg thiourea were dissolved in 20 ml deionized water under vigorous stirring to form a homogeneous solution. Then, the solution was transferred into a 30 mL Teflon-lined stainless steel autoclave and maintained at 220 °C for 18.0 h before the reaction system was allowed to cool to room temperature. The final product was washed with water and ethanol for several times to remove any possible ions and finally dissolved in ethanol.

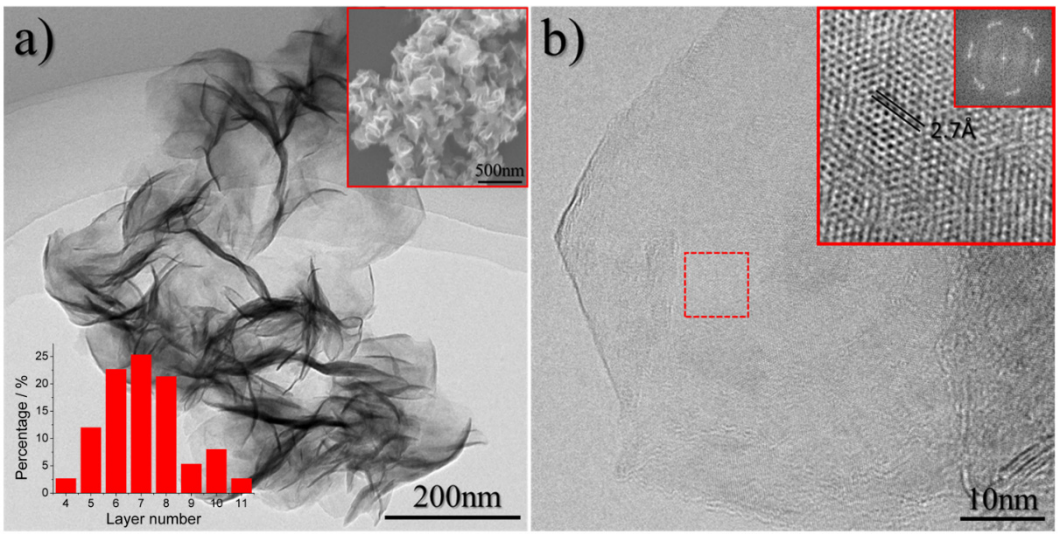

Figure S5. Characterization of defect-rich MoS_2 nanosheets; (a) TEM image of DR-MoS_2; inset of (a) shows the statistic layer number and the SEM image. (b) Magnified TEM, HRTEM and corresponding FFT images.

The inset of Figure S5b shows that the corresponding fast Fourier transform (FFT) pattern of the selected area contains six independent diffraction arcs, which is characteristic neither of a single crystal with six diffraction spots nor of a polycrystal in the form of diffraction cycles. This interesting observation can be attributed to the quasiperiodic structure that arises from the existence of rich defects.[11]

5. *Synthesis, characterization and the exploration of the formation mechanism for Pd nanodisks:*

5.1 Synthesis of Pd nanodisks:

In a typical synthesis, 50 mg of $Pd(acac)_2$, 160 mg of PVP and 185 mg of CTAB were mixed together with 12 ml mixture of DMF and water (volume ratio = 5:1). The resulting homogeneous yellow solution was transferred to a 25 mL Schlenk flask then charged with gas mixture of CO and air (volume ratio=1:1) to 1 bar and heated at 100 °C for 3.0 h before it was cooled to room temperature. The black products were precipitated by acetone, separated via centrifugation and further purified by an ethanol-aqua mixture and finally dissolved in ethanol.

5.2 Synthesis of hexagonal Pd nanoplates:

In a typical synthesis, 50 mg of $Pd(acac)_2$, 160 mg of PVP and 185 mg of CTAB were mixed together with 12 ml mixture of DMF and water (volume ratio = 5:1). The resulting homogeneous yellow solution was transferred to a 25 mL Schlenk flask then charged with gas mixture of CO to 1 bar and heated at 100 °C for 3.0 h before it was cooled to room temperature. The black products were precipitated by acetone, separated via centrifugation and further purified by an ethanol-aqua mixture and finally dissolved in ethanol.

5.3 Synthesis of Pd polyhedral:

In a typical synthesis, 50 mg of $Pd(acac)_2$, 160 mg of PVP and 185 mg of CTAB were mixed together with 12 ml mixture of DMF and water (volume ratio = 5:1). The resulting homogeneous yellow solution was transferred to a 25 mL Schlenk flask then charged with gas mixture of air to 1 bar and heated at 100 °C for 3.0 h before it was cooled to room temperature. The black products were precipitated by acetone, separated via centrifugation and further purified by an ethanol-aqua mixture and finally dissolved in ethanol.

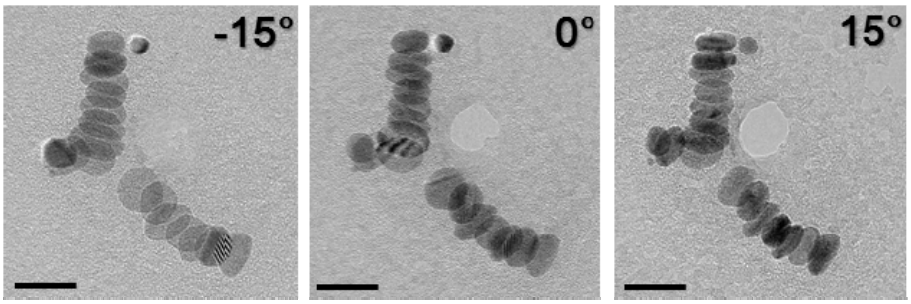

Figure S6. TEM images Pd nanodisks with different rotation angles. (Scale bars: 20 nm)

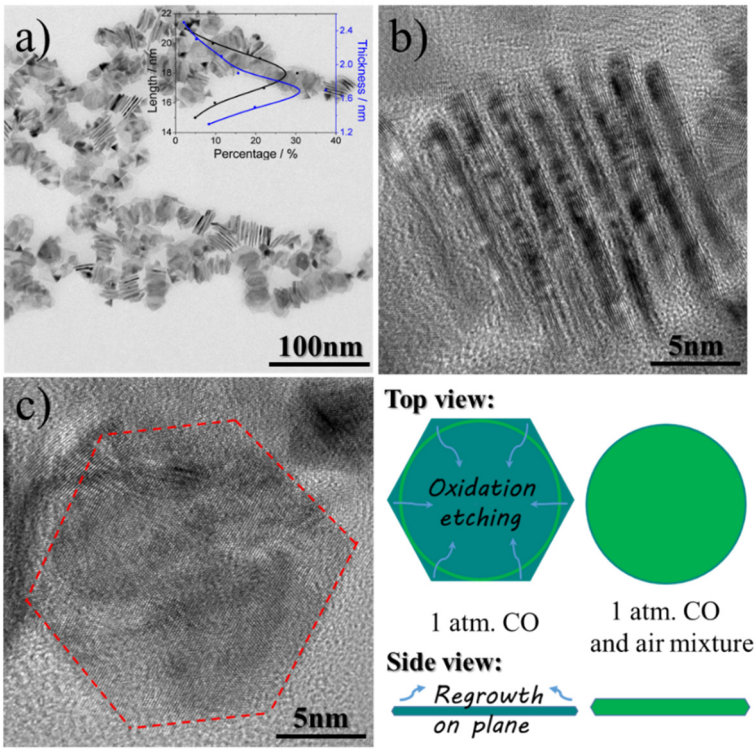

Figure S7. (a) TEM and (b-c) HRTEM images of Pd hexagon nanosheets (HNSs) synthesized in 1 atm. CO; inset in (a) shows the statistics data of diameter and thickness of Pd HNSs is of 18.5 and 1.65 nm, respectively. (b-c) shows HRTEM of two Pd nanosheets with distinct orientation recorded from side view and top view. (d) Proposed relationship between the formation mechanism of Pd HNSs and Pd NDs.

The synthesis of Pd hexagon nanosheets was previously reported by Zheng, with 1 atm. carbon monoxide act as both reductant and capping agent.[12] Due to the geometrical inscribe relationship between Pd nanodisks reported in this work and Pd hexagon nanosheets, Pd nanodisks are thicker than Pd hexagon nanosheets as well, we summarize the mechanism: oxidation etching at corners and regrowth on the plane surface, which can be clearly illustrated from Figure S7.

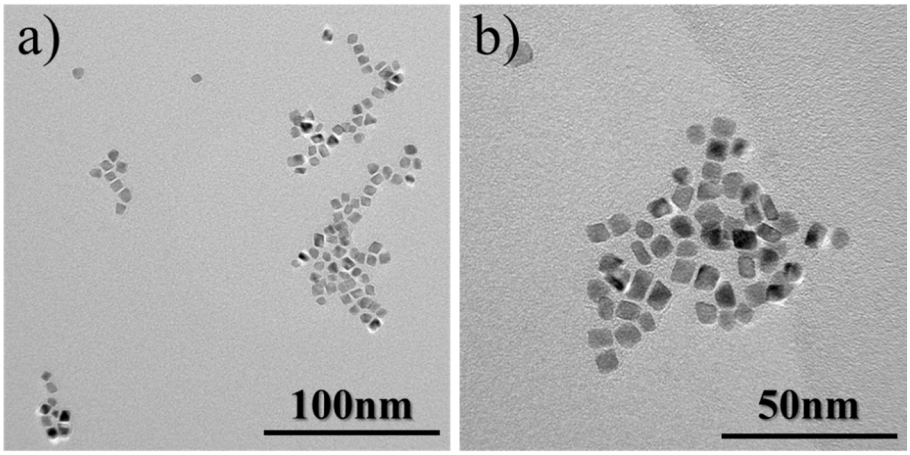

Figure S8. TEM images of Pd polyhedral synthesized in 1 atm. air.

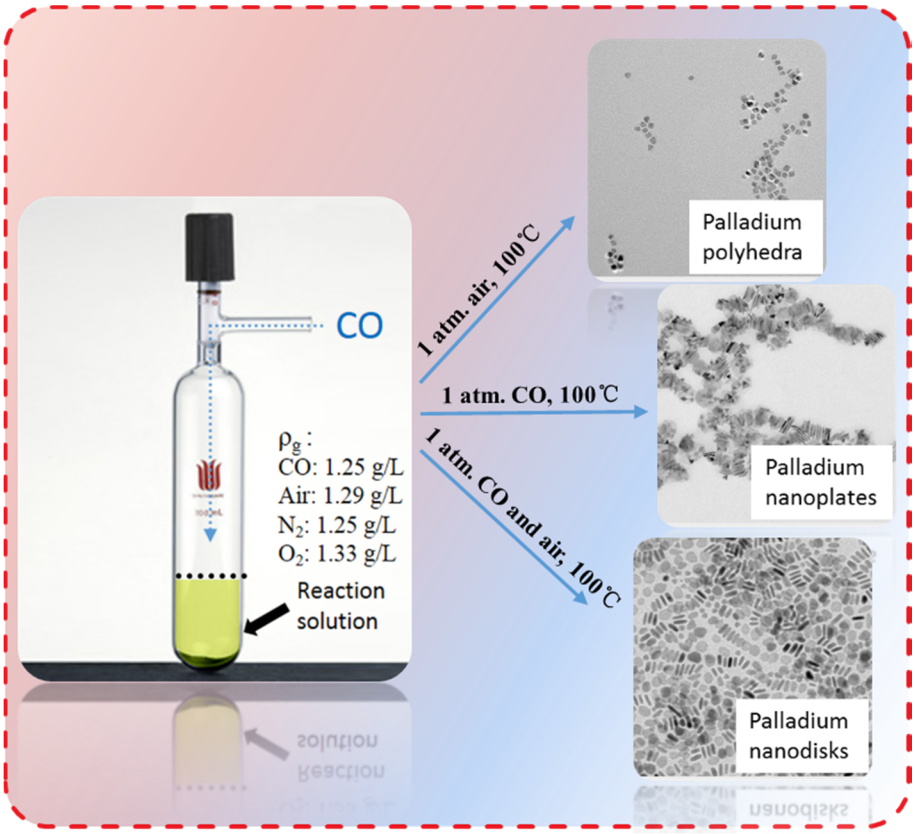

Figure S9. Routes for the synthesizing of Pd nanostructures with different morphologies by adjusting the volume ratio between CO and air.

6. *Assembly of Pd nanodisks on MoS_2 nanosheets:*

In a typical synthesis, 300 μL MoS_2 (31.25 mM in ethanol) and 300 μL Pd nanodisks (5.56 mM in ethanol) were dissolved by 10 mL ethanol in a glass vial with vigorously shocking. Then the vial was transferred to a constant temperature ultrasonic system with sonication for 36.0 h.

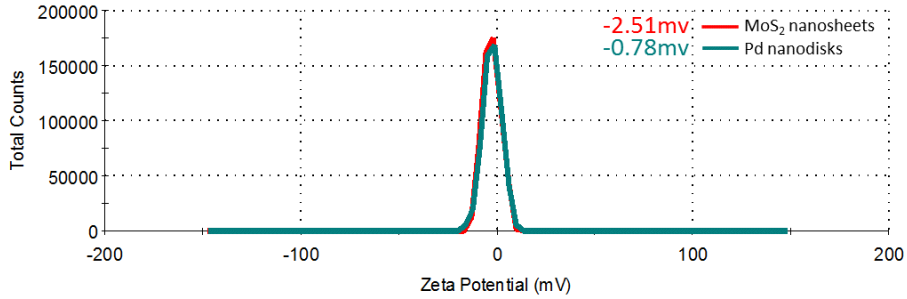

Figure S10. Zeta-potential of Pd nanodisks and defect-rich MoS_2 nanosheets shows that both Pd nanodisks and DR-MoS_2 are nagetively charged.

As can be seen from Figure S10, both Pd NDs and DR-MoS_2 nanosheets are negatively charged, to overcome the slightly electrostatic repulision, acting force is essential to be enforced.

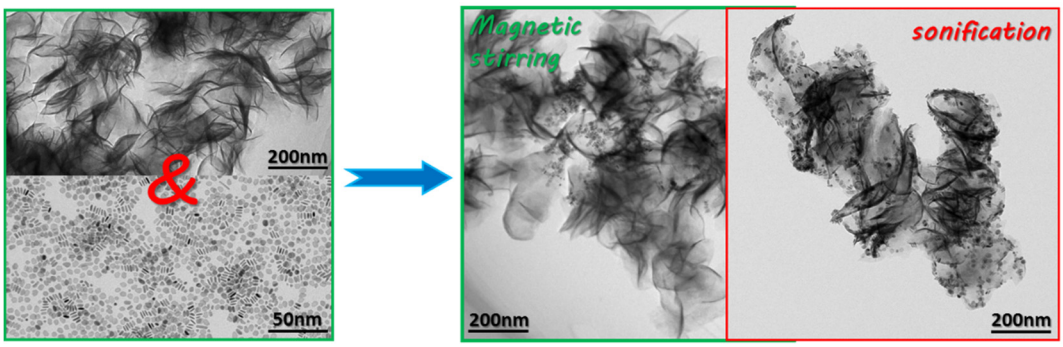

Figure S11. Strategies for the combination of Pd NDs and MoS_2 nanosheets. The results show that only magnetic stirring is not sufficient for the formation of Pd NDs and MoS_2 heterostructure. With the sonification, the Pd NDs were successfully assembled on MoS_2 nanosheets as indicated in the right image.

The lamellar structure of both MoS_2 and Pd NDs only cause weak Van der Waals interaction between two counterparts. The electrostatic repulsion between two parts may limit the

combination when magnetic stirring is adopted. To break this repulsion, extra energy of sonification was used for further improvement. The coefficient of Van der Waals pre-interaction and subsequent high-speed jets or intense shock waves induced by cavitation may generate the chemical bonding between Pd NDs and DR-MoS_2 (strong covalent bond is supposed to be easily formed between Pd and S atoms). The results show that sonification acquired the ideal heterostructure with uniform Pd NDs distribution

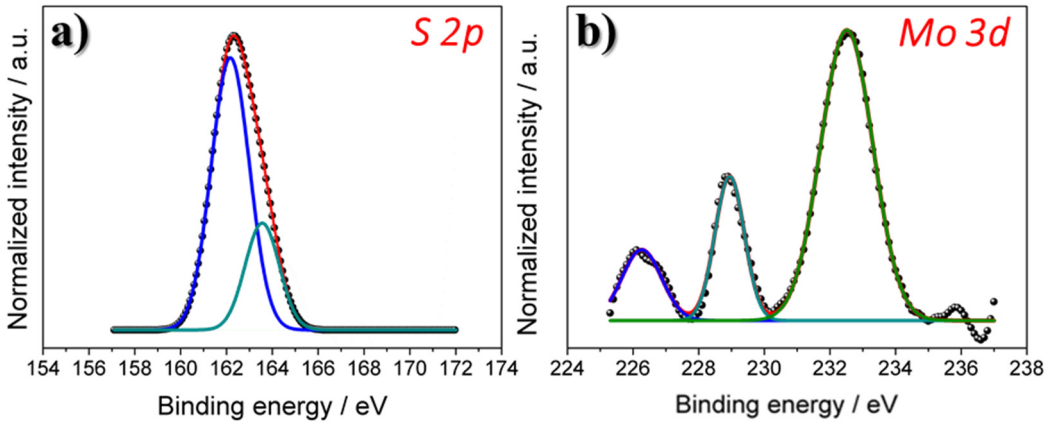

Figure S12. S 2P and Mo 3d XPS spectra of defect-rich MoS_2 nanosheets (without Pd nanodisks modification) after sonification.

By comparing between the XPS spectra shown in Figure 6 and Figure S12, we found that the combination of Pd nanodisks and MoS_2 nanosheets by sonification can change both the surface state of these two monomers, which can be attribute to the formation of covalent bond between Pd and S during sonification. However, as shown in Figure S12, the control experiment of sonification for MoS_2 in the absence of Pd nanodisks shows negligible change of the surface states of both S 2P and Mo 3d, indicating that only sonification didn't optimize the surface states of MoS_2 without Pd nanodisks modifying.

7. Electrochemical measurements and further characterizations after stability tests:

The electrochemical measurements were conducted by using a CHI650D electrochemical workstation (Shanghai, Chenhua Co., China). Typically, A three-electrode cell was used, for the fabrication of working electrode (WE), solution contains 20 μg of catalyst was loaded onto a glass carbon (GC) electrode with 3 mm diameter (loading ca. 0.285 mg cm^{-2}), then 1.5 μL of Nafion-ethanol solution (0.05 % wt.) was dispersed onto the surface of the GC electrode. An Ag/AgCl (in 3 M KCl solution) electrode was used as the reference electrode, a platinum foil electrode (1cm×3cm) as the counter electrode. All the potentials were calibrated to a reversible hydrogen electrode (RHE).

Before each electrochemical test, the electrode was electrochemical activated in a N_2 saturated 0.5 M H_2SO_4 solution by performing cyclic voltammetry scanning at 0.1 to -0.5 V for 50 cycles, after the cleaning process, stable voltammograms were obtained. Linear sweep voltammetry (LSV) was conducted in 0.5 M H_2SO_4 solution (saturated with N_2) between 0.1 and -0.6 V vs. RHE. Cyclic voltammetry (CV) was conducted between 0.1 and -0.3 V vs. RHE at 50 mV s^{-1} to investigate the cycling stability. The Nyquist plots were measured with frequencies ranging from 100 kHz to 0.1 Hz at an overpotential of 250 mV. All of the impedance data were fitted to a simplified Randles circuit to extract the series and charge-transfer resistances. Long-term stability test was recorded by taking a chronoamperometric curve at a constant overpotential of 150 mV. Onset overpotential was determined based on the beginning of linear regime in the Tafel plot. All data are presented without iR compensation. All of the electrochemical tests were performed at room temperature.

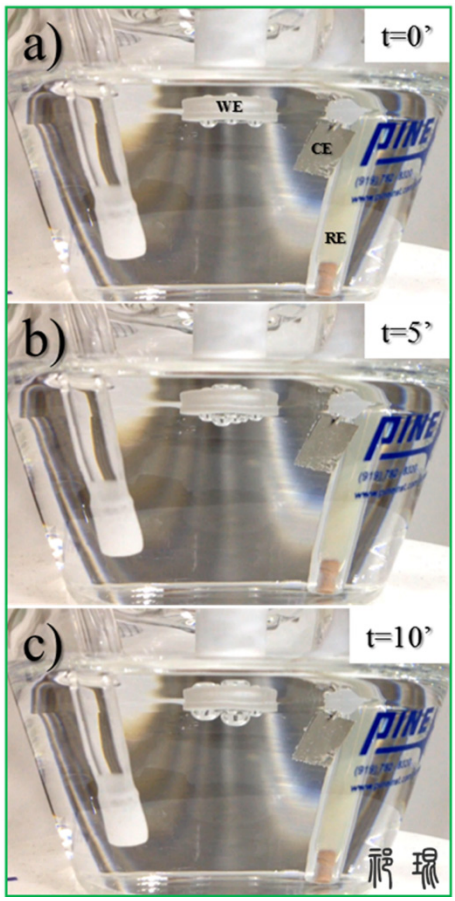

Figure S13. Optical photographs of the hydrogen bubbles generating from the glass carbon working electrode during the HER process at a statistic overpotential of 150 mV in 0.5 M H_2SO_4.

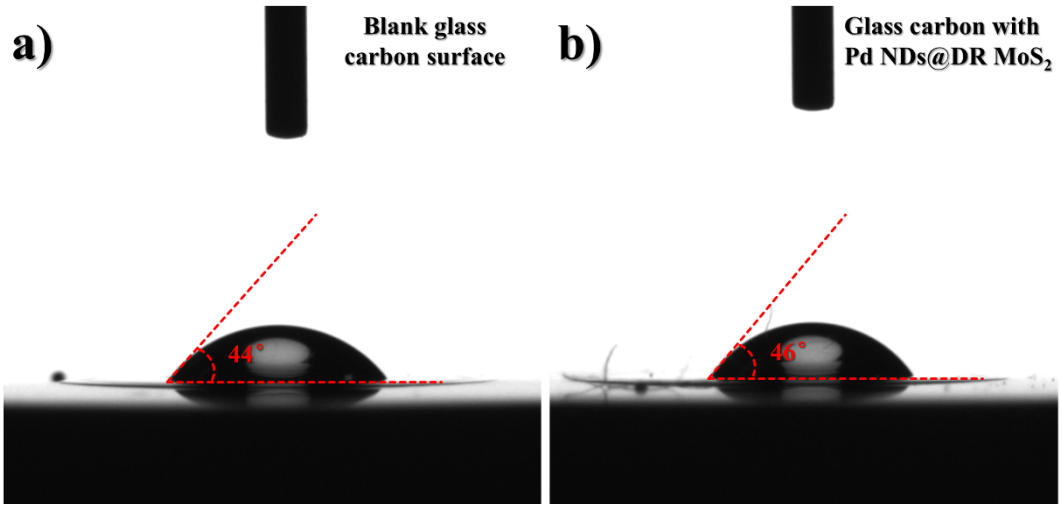

Figure S14. Wetting ability testing of a) Blank glass carbon surface (the contact angle was measured as 44°) and b) Glass carbon with Pd NDs/DR MoS_2 modified (the contact angle was measured as 46°). The wettability of the electrode surface by measuring the contact angles of 0.5 M H_2SO_4. For these experiments, 0.6 μL of the electrolyte was dropped on the film surface.

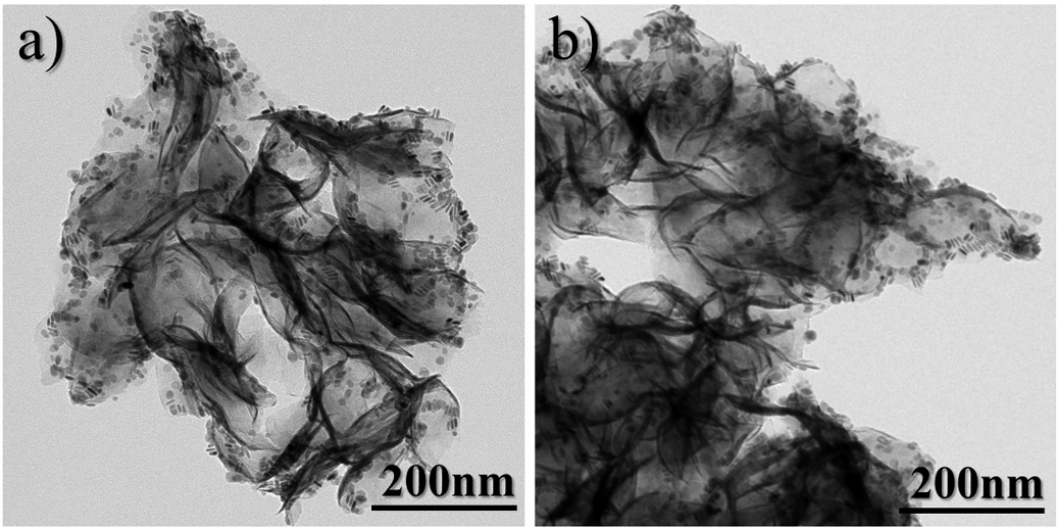

Figure S15. (a-b) TEM images of Pd NDs/DR-MoS_2 heterostructures (a) before and (b) after HER durability tests.

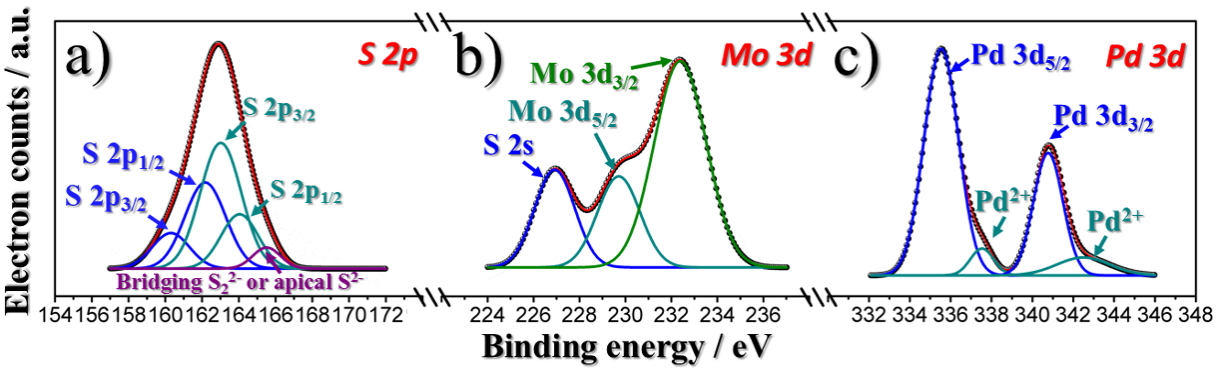

Figure S16. XPS spectra of Pd NDs/DR-MoS_2 after HER durability tests.

Table S3. HER parameters of various samples in this work.

Materials [a)]	Onset overpotential [mV]	Tafel slope [mV decade^{-1}]	Tafel region [mV]	j [mA cm^{-2}] [b)]
Pd NDs/DR-MoS_2	40	41	40-70	83
Pd NDs	249	59	249-284	13
DR-MoS_2	166	66	166-184	21
Pd/C	264	124	264-399	2
Pt/C	0	30	0-45	150

[a)]All the parameters were measured under the same conditions, i.e., catalyst loading weight of 0.285 mg cm^{-1} on glass carbon electrode in 0.5 M H_2SO_4 solution. [b)]Cathodic current density (j) was recorded at η = 300 mV.

Table S4. Calculations of the exchange current densities of various samples.

Materials	log(|j(mA cm^{-2}) at η=0V	Exchange current densities j_0[μA cm^{-2}]
Pd NDs/DR-MoS_2	-0.37	426.58
Pd NDs	-4.37	0.04
DR-MoS_2	-2.08	8.41
Pd/C	-2.66	2.19

Reference

1. B. Delley, *The Journal of chemical physics*, 1990, **92**, 508-517.
2. B. Delley, *The Journal of chemical physics*, 2000, **113**, 7756-7764.
3. J. P. Perdew, K. Burke and M. Ernzerhof, *Physical review letters*, 1996, **77**, 3865.
4. E. R. McNellis, J. Meyer and K. Reuter, *Physical Review B*, 2009, **80**, 205414.
5. B. Hinnemann, P. G. Moses, J. Bonde, K. P. Jørgensen, J. H. Nielsen, S. Horch, I. Chorkendorff and J. K. Nørskov, *Journal of the American Chemical Society*, 2005, **127**, 5308-5309.
6. J. Xie, J. Zhang, S. Li, F. Grote, X. Zhang, H. Zhang, R. Wang, Y. Lei, B. Pan and Y. Xie, *Journal of the American Chemical Society*, 2013, **135**, 17881-17888.
7. P. Raybaud, J. Hafner, G. Kresse, S. Kasztelan and H. Toulhoat, *Journal of Catalysis*, 2000, **189**, 129-146.
8. H. J. Monkhorst and J. D. Pack, *Physical Review B*, 1976, **13**, 5188.
9. D. Voiry, H. Yamaguchi, J. Li, R. Silva, D. C. Alves, T. Fujita, M. Chen, T. Asefa, V. B. Shenoy and G. Eda, *Nature materials*, 2013, **12**, 850-855.
10. Y. Wook Lee, M. Kim and S. Woo Han, *Chemical Communications*, 2010, **46**, 1535-1537.
11. J. Xie, H. Zhang, S. Li, R. Wang, X. Sun, M. Zhou, J. Zhou, X. W. D. Lou and Y. Xie, *Advanced Materials*, 2013, **25**, 5807-5813.
12. X. Huang, S. Tang, X. Mu, Y. Dai, G. Chen, Z. Zhou, F. Ruan, Z. Yang and N. Zheng, *Nature nanotechnology*, 2011, **6**, 28-32.